Toxicology and Applied Pharmacology 423 (2021) 115573

Contents lists available at ScienceDirect

Toxicology and Applied Pharmacology

journal homepage: www.elsevier.com/locate/taap

Delivery of oxaliplatin to colorectal cancer cells by folate-targeted UiO-66-NH_2

Alireza Hashemzadeh [a,b,c,1], Forouzan Amerizadeh [b,c,1], Fereshteh Asgharzadeh [a], Majid Darroudi [d], Amir Avan [b,c], Seyed Mahdi Hassanian [c], Mohammad Landarani [e], Majid Khazaei [a,c,*]

[a] Department of Medical Physiology, Faculty of Medicine, Mashhad University of Medical Sciences, Mashhad, Iran
[b] Department of Medical Biotechnology, Faculty of Medicine, Mashhad University of Medical Sciences, Mashhad, Iran
[c] Metabolic syndrome Research center, Mashhad University of Medical Sciences, Mashhad, Iran
[d] Department of Modern Sciences and Technologies, Faculty of Medicine, Mashhad University of Medical Sciences, Mashhad, Iran
[e] Faculty of chemistry, Shahid Beheshti University, Evin, 1983963113, Tehran, Iran

ARTICLE INFO

Keywords:
Metal-organic framework
microporous nanomaterials
smart drug delivery system host-guest interactions

ABSTRACT

Oxaliplatin is being used in different malignancies and several side effects are reported for patients taking Oxaliplatin, including peripheral neuropathy, nausea and vomiting, diarrhea, mouth sores, low blood counts, fatigue, loss of appetite, etc. Here we have developed a targeted anticancer drug delivery system based on folate-conjugated amine-functionalized UiO-66 for the delivery of oxaliplatin (OX). UiO-66-NH_2 (U) and UiO-66-NH_2–FA(FU) were pre-functionalized by the incorporation of folic acid (FA) into the structure via coordination of the carboxylate group of FA. The FTIR spectra of drug-loaded U and FU showed the presence of new carboxylic and aliphatic groups of OX and FA. Powder X-ray diffraction (PXRD) patterns were matched accordingly with the reference pattern and FESEM results showed semi-spherical particles (115–128 nm). The evaluated amounts of OX in U and FU were calculated 304.5 and 293 mg/g, respectively. The initial burst release of OX was 15.7% per hour for U(OX) and 10.8% per hour for FU(OX). The final release plateau gives 62.9% and 52.3% for U(OX) and FU(OX). To evaluate the application of the prepared delivery platform, they were tested on colorectal cancer cells (CT-26) via MTT assay, cell migration assay, and spheroid model. IC_{50} values obtained from MTT assay were 21.38, 95.50, and 18.20 μg/mL for OX, U(OX), and FU(OX), respectively. After three days of treatment, the CT26 spheroids at two doses of 500 and 50 μg/mL of U(OX) and FU(OX) showed volume reduction. Moreover, the oxidative behavior of the prepared systems within the cell was assessed by total thiol, malondialdehyde, and superoxide dismutase activity. The results showed that FU(OX) had higher efficacy in preventing the growth of CT-26 spheroid, and was more effective than oxaliplation in cell migration inhibition, and induced higher oxidative stress and apoptosis.

Abbreviations: dntb, 5,5′-dithiobis(2-nitrobenzoic acid); dmso, Dimethyl sulfoxide; tp, Terephthalic acid; u, Uio-66-nh_2; atp, 2-aminoterephthalic acid; microtracbel corp., japan, Belsorp-mini apparatus; crc, Colorectal cancer; ddss, Drug delivery systems; dls, Dynamic light scattering; chn, Elemental analysis; edx, Energy-dispersive x-ray spectroscopy; edta, Ethylenediaminetetraacetic acid; fesem, Field emission scanning electron microscopy; frs, Folate receptors; fa, Folic acid; ftir, Fourier transform infrared; frα, Fr alpha; fr+, Fr positive; hcl, Hydrochloric acid fuming 37%; 1hnmr, Hydrogen nuclear magnetic resonance; h_2o_2, Hydrogen peroxide; mofs, Metal-organic frameworks; dmf, N,n'-dimethylformamide; hno_3, Nitric acid 65%; ox, Oxaliplatin; Pbs, phosphate-buffered saline; pd, Pharmacodynamics; pk, Pharmacokinetic; pxrd, Powder x-ray diffraction; mtt, Pyrogallol, 3-[4,5-dimethylthiazol-2-yl]-2,5-diphenyltetrazolium bromide; sbus, Secondary building units; naoh, Sodium hydroxide; h_2so_4, Sulfuric acid 95–98%; tba, Thiobarbituric acid; $sncl_2.2h_2o$, Tin chloride dihydrate; tca, Trichloroacetic acid; tris, Tris (hydroxymethyl)aminomethane hydrochloride; fu, Uio-66-nh_2–fa; $zrcl_4$, Zirconium tetrachloride.

* Corresponding author at: Department of Medical Physiology, Faculty of Medicine, Mashhad University of Medical Sciences, Mashhad, Iran.
E-mail address: Khazaeim@mums.ac.ir (M. Khazaei).

[1] These two authors contributed equally to this work.

https://doi.org/10.1016/j.taap.2021.115573
Received 2 January 2021; Received in revised form 21 March 2021; Accepted 10 May 2021
Available online 13 May 2021

1. Introduction

Nanomedicine is aimed at delivering active agents to the cancer tissues and reduces the usual doses of medications (Onoue et al., 2014; Faust, 2015; Lazaro and Forgan, 2019). Chances of survival could be increased greatly by sustained-release dosage, using novel drug delivery systems (DDSs). The DDS efficacy (%) is contingent on several factors including physicochemical properties, pharmacokinetic (PK), pharmacodynamics (PD) and biocompatibility (Petrak, 2005; Rosenholm et al., 2010; Marcato, 2014). Improving drug efficacy provides a route 'to creative and effective therapies'. Metal-organic frameworks (MOFs), which were first introduced in the early 1990s, have been recognized recently as a means to improve the DDSs (Orellana-Tavra et al., 2015; Wu and Yang, 2017),. The interest was piqued to find more information about the spongy quality of MOFs on drug adsorption, PK, PD, biocompatibility, bioavailability, cytotoxicity, stability, and specificity (Ibrahim et al., 2017; Zangabad et al., 2017; Zhou et al., 2017). The skillful utilization of the high internal surface area lends interesting characteristics such as high drug loading to MOFs. The drug penetrates deep into the pores and displays an effective release profile. The encapsulation, which is promoted by specific modifications using physical or chemical means, leads to the elaboration of new release mechanisms and novel sustained or stimulus-responsive drug releases (Wu and Yang, 2017; Cai et al., 2019). MOFs are so flexible that can adapt to any changes required for specific goals, especially smart DDSs. Adjustments could be made by synthetic procedures, through pre/post-modifications over secondary building units (SBUs) or polytopic organic linkers (Cao et al., 2018a; Simagina et al., 2018). The evolution of targeted chemotherapy requires a precisely formulated master plan which employs overexpressed pathways in cancer cells (Singh et al., 2016; Yu et al., 2016; Clemons et al., 2018). In active targeting, the conjugated homing ligands bind to a receptor on cancer cells, devising strategies to produce the next class of anticancer agents (Kue et al., 2016). These ligands are used to deliver medications selectively into malignant cells. In this manner, drug-loaded MOFs conjugated with targeting agents could have higher drug potency against malignancies, which guide drug payloads through and diffuse across tumor cell membranes; presumably, drug discharge after internalization could prevent undesirable drug release into receptor-negative cells (Dai et al., 2016). Targeting is a contributing factor in selective internalization of enclosed potent chemotherapeutics to the specific cells. SDDSs (smart drug delivery systems) may offer slender hope to patients with high-grade cancers in third-line therapies and beyond, for instance, for metastatic or drug-resistant cancers (Moore et al., 2017; Moore et al., 2018). Hence to maximize the utility of DDSs and to find thoughtful solutions to treat cancer, an integrated drug-transport system composed of targeting agents is preferred, which may include monoclonal antibodies, peptides, aptamers, oligo-saccharides, and vitamins (Fan et al., 2012; Toporkiewicz et al., 2015; Wu et al., 2015).

Cancer might lead to changes in the protein expression depending on the type and stage of cancer. The changes in the level of expression of many cellular proteins while transforming to cancer cells promote a continued growth of cell proliferation and metabolism, which led to escaping from cell death messages (Bahrami et al., 2018). The favorable prognosis in most patients is diagnosed with the cancer stage and choosing the right treatment, hence new precautions are needed at advanced stages of the disease.

The folate receptors (FRs) are synthesized in abnormally large amounts in malignancies, especially colorectal, brain, breast, ovarian, and nervous system cancers (Weitman et al., 1994; Hartmann et al., 2007; Kalli et al., 2008; Markert et al., 2008; Li et al., 2016a). The FR alpha (FRα) is a cell membrane-anchored protein that has a high affinity to bind to folic acid (FA) and its conjugated nanoforms, which can target FR positive (FR+) cancer cells. The biological significance of FA (known as vitamin B_9 and folacin) is DNA biosynthesis and methylation (Sudimack and Lee, 2000).

The 5-year survival rate for colorectal cancer (CRC) patients is around 90% and 5% for stage I and stage IV, respectively. Many academics have researched the effect of FRα as a major biomarker for suppressing tumor proliferation in CRC (Zhang et al., 2012; Coppede, 2014; Varshosaz et al., 2014; Bansal et al., 2016). There are real issues of practical and systematic approaches in high-grade CRC treatment. The right way to resolve the matter could be FA-conjugated nano-vehicles/drugs (Boddu et al., 2012; Steichen et al., 2013; Chen et al., 2014; Khoshgard et al., 2014; Lai et al., 2014; Samadian et al., 2016). The advantages of FA conjugates are due to the higher cytotoxicity, higher cellular uptake, and the greater capacity to induce apoptosis. FA-functionalized MOFs have been also reported to be effective in the treatment of different cancers in both cellular and animal models (Au et al., 2016; Chowdhuri et al., 2017a; Chowdhuri et al., 2017b; Liu et al., 2017; Dong et al., 2018; Nejadshafiee et al., 2019).

In this study, we have shown a preliminary design of a new smart DDS for oxaliplatin (OX) which have an assembly of MOF features using an active targeting and the aim was to treat high-grade CRC in the future treatments. We used UiO-66-NH_2(U) and FA-conjugated UiO-66-NH_2 (FU) to deliver loaded OX to CT-26 cancer cells. The main goal of this study was to develop new effective nanodrugs for CRC cancer and compare the drug efficacy in FU and U in cellular models using the MTT assay, cell migration assay and spheroid models of cancer, and also their oxidative attributes.

2. Materials and methods

2.1. Instruments and materials

Energy-dispersive X-ray spectroscopy (EDX), EDX mapping and field emission scanning electron microscopy (FESEM) was carried out using a TESCAN Mira 3 LMU. Nitrogen adsorption-desorption isotherms were obtained with a BELSORP-mini apparatus (MicrotracBEL Corp., Japan). Fourier transform infrared (FTIR) spectra were obtained on an M-500 Fast-Scan IR spectrometer (Buck Scientific, USA). UV–Vis absorption measurements were recorded on a Cecil Instruments-9500 CE UV–Vis spectrophotometer. A Horiba SZ-100-Z was used to conduct dynamic light scattering (DLS) and measure zeta potentials. Sonorex Digitec DT 510 H was utilized for sonication and a STOE-STADV STAIP diffractometer for Powder X-ray diffraction (PXRD) measurements over the 2θ of 3–80° and Cu Kα radiation, λ = 1.54060 Å. Hydrogen nuclear magnetic resonance (1HNMR)

was taken by Bruker AVANCE3 3-300 MHz. Elemental analysis (CHN) was measured by a FLASH EA 1112 Series CHN analyzer using Eager 300 software. The cells were observed by Leica-DMI300B inverted phase-contrast microscope (Leica Microsystems GmbH, Wetzlar, Germany). Epoch microplate spectrophotometer was used for UV–Vis absorbance measurements in plate reading. Heidolph homogenizers SilentCrusher tool was employed for homogenizing. Analysis of the Pt was carried out by an inductively coupled plasma-optical emission spectrophotometer (ICP-OES; Spectro Arcos 7600/CRMA, Germany).

Oxaliplatin (OX), zirconium tetrachloride ($ZrCL_4$), terephthalic acid (TP), tin chloride dihydrate ($SnCl_2.2H_2O$), Thiobarbituric acid (TBA), folic acid (FA), oxaliplatin (OX), agarose gel, and PBS (Phosphate-Buffered Saline) Tablets were purchased from Sigma–Aldrich. Methanol, acetone, ethanol, hydrogen peroxide (H_2O_2), N,N′-dimethylformamide (DMF), dimethyl sulfoxide (DMSO), hydrochloric acid fuming 37% (HCl), sodium hydroxide (NaOH), nitric acid 65% (HNO_3), sulfuric acid 95–98% (H_2SO_4), pyrogallol, 3-[4,5-dimethylthiazol-2-yl]-2,5-diphenyltetrazolium bromide (MTT), 5,5′-Dithiobis(2-nitrobenzoic acid) (DNTB), tris(hydroxymethyl)aminomethane hydrochloride (TRIS), ethylenediaminetetraacetic acid (EDTA) and trichloroacetic acid (TCA) were obtained from Merck chemical company. All the starting reagents and solvents were of analytical grade. 2-aminoterephthalic acid (ATP) was synthesized as described previously (Li et al., 2014).

CT26 / CRC cell is a murine colorectal carcinoma cell line which is

from a BALB/c mouse. The cell is a clone of the N-nitroso-N-methylrethane-induced undifferentiated CT26 colon carcinoma cell line. These cells are adherent and have a fibroblast morphology. They will form tumors and metastases post implantation into syngenic BALB/c mice or immunocompromised mice. Cell culture was performed in a T25 flask using CT26 cell line (from ATCC, Manassas, VA, USA) at 37 °C under 5% CO_2 humidified atmosphere using RPMI:DMEM composing of 1% streptomycin/penicillin and 10% FBS. Eventually, in their exponentially growing phase, at 70%–80% confluence Routine passaging was accomplished by using trypsin-EDTA of cells (Hashemzehi et al., 2021). The oxidative stress was evaluated in the recovered ~3 × 10^6 CRC cells in PBS (1 mL, 0.01 M, pH = 7.4). Cells were homogenized on ice and indexes of malondialdehyde (MDA), total thiol (T-SH) and superoxide dismutase (SOD) were measured.

2.2. Synthesis of 2-aminoterephthalic acid (ATP)

A three-necked round-bottom flask was charged with 20 g of TP and sulfuric acid (60 mL, 95–98%). Then, nitric acid (15 ml, 65%) was added slowly over an hour with stirring at 0 °C. The reaction temperature was increased gradually until the temperature of 60 °C was reached. It was maintained over 1 h at this temperature, then increased gradually over 80 °C in 1 h and held at this temperature overnight. Thereafter, the mixture was cooled by pouring ice water into the reaction vessel. The product was filtered and washed with 3 l of distilled water. The filtrate was recrystallized in 1 l of acetone to obtain 2-nitroterephthalic acid (NTP). Acetone could dissolve NTP, but not the precursor (TP). The precipitate was filtered and dried in the oven at 60 °C. To reduce the nitro group, eighty milliliters of hydrochloric acid fuming 37% was added to a three-necked round-bottomed glass and tin chloride dihydrate (30 g) was added gradually to the flask with stirring. Thereafter, 10 g of NTP was added to the suspension and reacted at 80 °C for 6 h. After the reaction, the mixture was filtered with distilled water and the precipitate was dried in an oven for 2 h at 60 °C to form ATP. Color: lemon yellow powder (yield: 9.83 g, 45%); m.p. >300 °C; ^{1}H NMR (300 MHz, DMSO-d_6) δ = 7.79 (d, 1 H, aromatic CH), 7.41 (d, 1 H, aromatic CH), 7.04 (dd, 1 H, aromatic CH), 9.68 (s, 2H, COOH).

2.3. Synthesis of UiO-66-NH_2 (U) and FA-UiO-66-NH_2 (FU)

The syntheses of U and FU were performed using a solvothermal process (Katz et al., 2013). Briefly, a 100 mL round-bottom flask was charged with 0.5 g of $ZrCl_4$, 20 mL of DMF and 4 mL of HCl (37%) and another flask was charged with 0.536 g of ATP and 40 mL of DMF;the mixtures then were sonicated for 20 min. In the case of FU, the latter solution does also include 5, 15, and 25 mol% of FA relative to the metallic precursor (Table 1). The product respectively would be called FU_5, FU_{15} and FU_{25}. Thereafter, the ligand solution was added to the $ZrCl_4$ solution and the mixture was sonicated for an additional 20 min before being heated at 80 °C for a period of 36 h under autogenous pressure conditions using a 100 mL Teflon-lined stainless steel autoclave. After cooling to room temperature, the products were collected by centrifugation (4000 rpm, 5 min) and were washed with DMF (2 × 30 mL) and methanol (3 × 30 mL). As-synthesized U and FU were soaked in 20 mL of CH_2Cl_2, 3 times over 1 h (20 min each),. Then, were immersed in 20 mL of dry n-hexane over 1 h, followed by solvent evacuation at 100 °C for 24 h. The PXRD analysis showed the FU_{25} was not formed and the FU_{15} would be used from now on, which would be named FU, in all the experiments. Elemental analysis (wt%): Calc. for U ($Zr_6O_4(OH)_4(ATP)_6$): C, 32.87; H, 2.28; N, 4.78; found: C, 31.94; H, 3.39; N, 5.20; found for FU(5%): C, 32.87; H, 3.09; N, 5.71, and for FU (15%): C, 35.34; H, 2.78; N, 7.07.

2.4. Loading Oxaliplatin (OX)

A 30 mg sample of U or FU had dispersed 12 mL of OX solution in distilled water (c = 5 mg/mL). After stirring for 48 h under dark conditions, the OX-loaded U or FU was centrifuged (4000 rpm, 5 min). After centrifugation, the obtained products were washed with 15 mL distilled water several times until the supernatant solution had no signal of OX using UV–Vis spectroscopy. The OX-loaded U and FU were used for subsequent in vitro tests against CT-26 cells. To evaluate the OX-loading efficiency, the supernatant and washed solutions were collected and the residual OX content (ROX) was measured by using UV measurement at the wavelength of 252 nm. The loading efficiency % (LE%) of OX can be calculated as follows: LE% = (OOX - ROX)/OOX) × 100%, in which OOX is the original OX content and (OOX - ROX) is the mass of OX loaded into U or FU.

2.5. In vitro drug release

To study the OX release profile at different time intervals, six samples of 5 mg drug-loaded of MOF were re-dispersed in 1 ml distilled water (initial pH = 5.5). The suspensions were incubated at 37 °C. UV–Vis spectroscopy was used to measure the amount of drug release after 1, 3, 6, 12, 24, and 48 h. After incubation, the suspensions were centrifuged and the supernatants were used for further analysis.

2.6. Growth inhibition evaluation

The cell growth inhibitory activity of OX, U, FU, U(OX) and FU(OX) was determined by the MTT assay. In detail, 5106 cells were seeded into 96-well plates and incubated for 24 h. Subsequently, various concentrations of U, FU (1–1000 μg/mL), or OX (0.001–1000 mM) were administered for 24 h to find cell viability. Analyses were performed as described previously [37].

2.7. Scratch assays

Cell migratory behavior of OX, U(OX) and FU(OX) against CT-26 cells (seeded cells = 1 × 10^5/well) were evaluated in 24-well plates and the surface of the plates were marked by a yellow Pipette tip. After

Table 1
Synthesis conditions (amount and concentration of solutes and solvents, and reaction temperature, and reaction time).

	2-aminoterephthalic acid (ATP) (mg)	$ZrCl_4$ (mg)	HCl (mL)	DMF (mL)	Folic acid (FA): ZrC14 mole ratio	Synthesis Temperature (°C)
UiO-66-NH2	536 (3.00 mmol)	500 (0.216 mmol)	4	60	–	80
FA_5-UiO-66-NH2	536 (3.00 mmol)	500 (0.216 mmol)	4	60	0.05:1	80
FA_{15}-UiO-66-NH2 (FU)	536 (3.00 mmol)	500 (0.216 mmol)	4	60	0.15:1	80
FA_{15}-UiO-66-NH2	536 (3.00 mmol)	500 (0.216 mmol)	4	60	0.25:1	80

Reaction time: 36 h.

that, the Cells were treated with 20 μM OX, 500 μg/mL U(OX) and FU (OX), and were compared with control. ImageJ version 1.52a (National Institutes of Health, Bethesda, MD, USA) was used to measure changes in the emerged edges.

2.8. Multicellular spheroids formation

Spheroids were developed and OX, U(OX) and FU(OX) were treated against CT-26 cells. Briefly, spheroids with a density of 5×10^4 cells/well in DMEM/F12 + GlutaMAX-I (1:1) were cultured in agarose-coated 96 well plates and subsequently treated with 8 μg/mL OX, 50 and 500 μg/mL of U(OX), and 50 and 500 μg/mL of FU(OX). The cytotoxic effects were assessed for 3 days on the inverted phase-contrast microscope. Finally, spheroid size changes were analyzed by ImageJ version 1.52a (National Institutes of Health, Bethesda, MD, USA).

2.9. Measurement of oxidant indicator

Changes of MDA concentration, an index of lipid peroxidation, was measured as described previously(Asgharzadeh et al., 2017). First, HCl (2 mL,37%), TBA (0.375 g) and TCA (15 g) were brought to a volume of 100 mL by distilled water and a volumetric flask, then, 600 μl was charged into a suspension of CT-26 cells. Next, the solution was incubated in a water bath for 40 min. Then, it was cooled and centrifuged (1500 rpm, 5 min). Finally, the absorbance was read at $\lambda_{max} = 535$ nm by a UV–Vis spectrophotometer. The MDA concentration, C(m), was calculated by the following equation: C (m) = Absorbance / (1.65×10^5).

2.10. Measurement of antioxidant indicator

2.10.1. Total thiol groups (T-SH)

The antioxidant activity was measured by analyzing T-SH content (Bargi et al., 2017). In detail, 50 μL of the sonicated CT-26 cells were added to 1 mL TRIS-EDTA (TE) buffer (pH = 8.6). The buffer was made from TRIS-HCl (3 g), EDTA (0.05 g) in a volume of 100 ml distilled water using a volumetric flask. Then, the absorbance was read at $\lambda_{max} = 412$ nm against TE buffer alone (A1). Next, the homogenized cells were added to a 20 μL solution of DTNB (0.04 g) in methanol (10 mL). After 15 min, the absorbance was read at $\lambda_{max} = 412$ nm again (A2). The DTNB absorbance was used as the blank (B). Finally, T-SH content, c(T-SH), was measured with the following equation: $c(T\text{-}SH) = (A2 - A1 - B) \times 1.07/0.05 \times 13.6$.

2.10.2. Superoxide dismutase (SOD) activity assay

SOD activity was measured according to the reported method by Madesh and Balasubramanian (Madesh and Balasubramanian, 1998). In this approach, one unit of SOD was evaluated as the amount of enzyme required to inhibit the rate of MTT reduction by 50%. First, pyrogallol (0.001 g) and MTT (0.005 g) solutions in distilled water (10 mL) were made using a volumetric flask (10 mL). Then, the homogenized cells were poured into the wells containing the above solution and incubated at room temperature for 5 min. Then, DMSO stopped the reaction (150 μl). Finally, the SOD activity was calculated at $\lambda_{max} = 570$ nm using a UV–Vis spectrophotometer. The results were shown as unit/ml of the homogenate cells.

3. Result and discussion

MOFs malleability in design, especially tuning the surface properties and pores, and advantages like high surface area and biocompatibility may resolve many issues in DDSs such as toxicity, drug loading, and uncontrolled drug release (Horcajada et al., 2010; Miller et al., 2010; Wu and Yang, 2017). A list of known MOFs with their drug composition and targeted cancer cell lines used in folate-based DDSs are presented in Table 2. In most cases, non-toxic and biocompatible families of MOFs including ZIFs, Zr-based MOFs like UiOs and MOF-808, Fe-based MILs, IRMOFs and Bio-MOFs are used in the design of DDSs which are based on folic acid as the targeting ligand. The stability and the intrinsic characteristics of MOFs differ with their composition. As a result, a collection of MOFs can be used to design different delivery systems with specific aims. There would be a variety of choices if MOFs were available for use in biomedical applications. Functionalization of DDSs with targeting ligands could improve the chemical or dispersion stability, cell-membrane crossing and invisibility to macrophages (Zucolotto, 2013; Abánades Lázaro et al., 2018b). The developed nanocomposites have provided a promising platform in DDSs to treat different cancers (Table 2). Table 2 summarized almost all the folate targeted MOFs in

Table 2
Folic acid conjugated MOFs in cancer treatment.

MOF Family	MOF Type	Drug composition	Cell Line	Ref.
ZIFs	ZIF-8	DOX[a]@ZIF-8-FA	HepG2 cells	(Jiang et al., 2018)
		Quercetin@FA[b]-BSA[c]-CuS-ZIF-8	B16F10 cells	(Chowdhuri et al., 2017a)
		5-FU[d]@ FA-CS[e]-5-FAM[f]-ZIF-8	MGC803 cells	(Gao et al., 2016)
		DOX-VER[g]@ZIF-8-PEG[h]-FA	FR-positive B16F10 & MCF-7/A cells	(Zhang et al., 2017b)
		5-FU@UCNP[i]-ZIF-8-FA	HeLa and L929 cells	(Chowdhuri et al., 2016b)
MILs		5-FU@MIL-53-NH_2-FA-5-FAM	MGC-803 and HASMC cells	(Gao et al., 2017)
UIOs	UIO-66	DOX@UCNP-UIO-66-NH_2-FA	TNBC cells (MDA-MB-468) and NIH3T3 cells	(Chowdhuri et al., 2017b)
		DCA[k]@Zr-fum-FA	HeLa and MCF-7 cancer cells	(Abánades Lázaro et al., 2018a)
		5-FU@ppy[l] -UiO-66-WP6-PEI − FA	L02 and HeLa cells	(Wu et al., 2018)
		5-FU@UIO-66-NH_2-FA-5-FAM	HepG-2 cells	(Gao et al., 2018)
		DCA@UiO-66-FA	MCF-7 and HEK293 cells	(Abánades Lázaro et al., 2018b)
		5-FU@UIO-66-NH_2-FA	HeLa and L929 cells	(Dong et al., 2018)
	UIO-68	DOX@UiO-68-FA	HepG-2 cells	(Li et al., 2016b)
IRMOFs	IRMOF-3	Pac[m]@IRMOF-3-FA	HeLa and NIH3T3 cells	(Chowdhuri et al., 2016a)
		DOX@Fe_3O_4-OCMC-IRMOF-3-FA	HeLa and L929 cells	(Chowdhuri et al., 2016c)
		5-FU@IRMOF-3-FA	HeLa, A549 and KB cells	(Yang et al., 2017)
		Cur[n]@IRMOF-3-FA	TNBC cells	(Laha et al., 2019)
Other MOFs	MOF-808	5-FU@FA-MOF-808	HeLa and L929 cells	(Dong et al., 2018)
	Bio-MOF	5-FU@Fe3O4-bio-MOF-CS-FA	MDA-MB-231 and NIH-3 T3 cells	(Nejadshafiee et al., 2019)

[a] DOX (doxorubicin).
[b] FA (folic acid).
[c] BSA (bovine serum albumin).
[d] 5-FU (5-fluorouracil).
[e] CS (chitosan).
[f] 5-FAM (5-Carboxyfluorescein).
[g] VER (verapamil hydrochloride).
[h] PEG (pegylated).
[i] UCNP (up-conversion nanoparticle).
[k] DCA (dichloroacetate).
[l] ppy (polypyrrole nanoparticle).
[m] Pac (Paclitaxel).
[n] Cur (Curcumin).

different cell lines such as liver, melanoma, breast, human gastric cancers, etc. The effect of drug delivery by folate conjugated MOFs showed better performance than drugs. Drug delivery systems via active targeting by folic acid are reliable, efficient and affordable. It appears ZIF-8 and UiO-66 are the most used MOFs that are conjugated with folic acid. In the case of ZIF-8, the most mechanism used in synthesis is in situ self-assembly of ZIF-8 with other ingredients such as drugs or targeting agents. It encapsulates the active ingridients inside and releases by biodegradation over time. Some MILs, such as MIL-100, could also have a similar mechanism in the release. On the other hand, MOFs such as UiO-66 are ideal nano-vehicles for oral delivery due to their slow degradation and high chemical stability in a phosphate solution, which works for colon-specific drug delivery. Although targeting agents are clinically approved in CRC, there are still many challenges toward targeted therapy including diagnostic tools, toxicity and costs The investigation of new effective SDDSs for CRC patients could improve treatments. Several studies have used a pool of diverse nanoparticles to introduce new therapies with a better efficacy, a quicker treatment period, and ability to reduce the neurotoxicity of OX or other side effects (Brown et al., 2010; Handali et al., 2019; Nguyen et al., 2019). To the best of our knowledge, there were no studies to focus on the comprehension of the OX encapsulation into MOFs and its related delivery processes in CRC, which is crucial to be improved. We introduced an effective DDS to eradicate CRC cells by combining U with folic acid (FA) and enhancing the internalization process in CRC cells (Fig. 1,**A**). Zr-based MOFs such as UiOs have higher stabilities than other MOFs and are biocompatible and efficient DDSs in cellular or animal models (Bai et al., 2016). In particular, the ability of UiO-66 to penetrate cell walls (Orellana-Tavra et al., 2016a, 2016b) together with its degradability in phosphate medium (Orellana-Tavra et al., 2016a, 2016b) makes it a good candidate for folic acid-based DDSs. For instance, Abánades Lázaro used a PEGylated analog of UiO-66 (Zr-fum) and UiO-66 against HeLa and MCF-7 cancer cells, which were well tolerated by HEK293 kidney cells, J774 macrophages, and human peripheral blood lymphocytes (Abánades et al., 2018). Moreover, the amine-functionalized UiO-66 could be regarded as an even better drug carrier than conventional ones in which numerous amino groups of U or FU can be used to control over drug loading and release due to hydrogen bonding, giving rise to DDSs with functionalities for biological applications.

FA and FA conjugates could attach to FR that is overexpressed by CRC CT-26 cells (Fig. 1,**A**). The aim of active targeting is to use receptor internalization and to improve the cellular uptake (Abánades Lázaro et al., 2018a; Wu et al., 2018). Healthy cells are less prone to FA uptake than CRC cells, which are FR+. In fact, a subset of CRCs actually have this characteristic, and overexpression occurs in approximately 30–40% of human CRC tissues, FA can be used in theses conditions (Shia et al., 2008; D'angelica et al., 2011). FA is essential in one-carbon (1C) metabolism and biosynthesis of nucleotides, which are essential for cancer growth (Sudimack and Lee, 2000). Overexpression of the alpha isoform of FR (FRα) in cancers, especially CRC cells, is the most important reason for using folic acid as a targeting agent. Therefore, FU would have the ability to be internalized after binding to CRC cells via clathrin-mediated endocytosis. In this strategy, FU could result in the direct killing of CRC cells, but not the healthy ones.

In this research, a one-pot synthesis for direct incorporation of FA into U was used. According to the previous reports, free carboxylic acids in FA can bind to the $[Zr_6O_4(OH)_4]$ clusters (Fig. 1,**B**) (Abánades Lázaro et al., 2018b). Different amounts of FA were used to reach the optimal composition, and 15% FA doping was selected via PXRD and CHN analyses. CHN analyses showed that the contents of nitrogen and carbon were increased due to the incorporation of folic acid.

FTIR spectra of the F, OX, U, FU, U(OX) and FU(OX) were shown in Fig. 2,**A.** The presence of new peaks demonstrated the changes over FU, U(OX) and FU(OX) that was compared to U, FA and OX. In FT-IR spectroscopy, the peak of FA at 3232 cm^{-1} was related to NH_2 group, at 1693 cm^{-1} was associated with ν(COOH), at 1614 and 1622 cm^{-1} were ascribed to ν(N-H) bending vibrations and at 1483 cm^{-1} was related to the vibration of the phenyl ring (Thu et al., 2015; Nam et al., 2016). FU showed the peaks at 3232 and 1639 cm^{-1} that corresponded to amine and carboxylate groups in FA, which could not be observed in U. Characteristic peaks of OX appeared between 2860 and 2990 cm^{-1} that was related to $\nu(CH_2)$ of oxalate ligand. The other peak at 3087 cm^{-1} was associated with $\nu(NH_2)$ (Agrahari et al., 2017). Oxalate ligand also showed characteristic peaks of $\nu(COO^-)_{sym}$ and $\nu(COO^-)_{asym}$ at

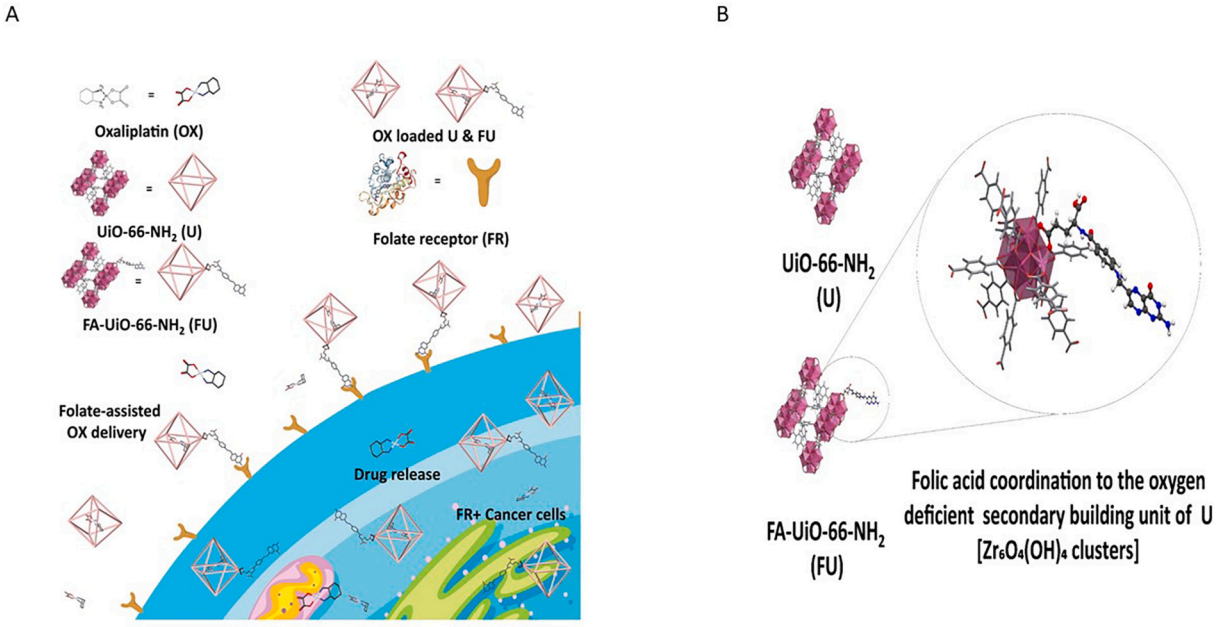

Fig. 1. Attachment and internalization of FA-conjugated MOFs to FRα that is overexpressed by CRC CT-26 cells in proportion with Free MOF (A). Combining U with folic acid (FA) as a targeting agent (B).

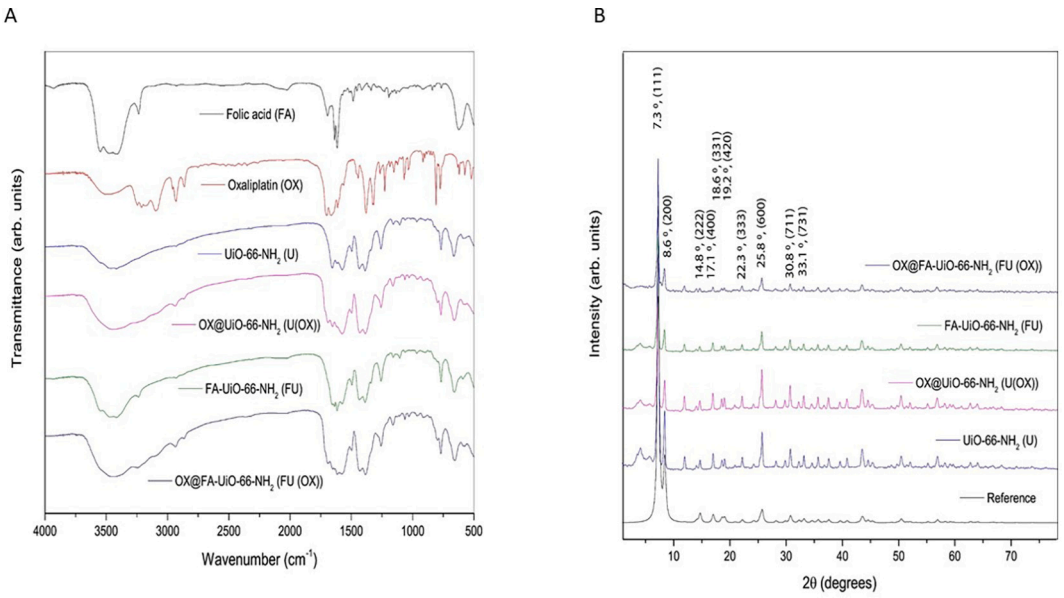

Fig. 2. FTIR spectra of U, FU, U(OX), and FU(OX) in comparison with FA and OX (A). PXRD of U: UiO-66-NH_2, U(OX): loaded U with OX FU: UiO-66-NH_2-FA, FU (OX): loaded FU with OX in comparison with simulated pattern with reference code of RUBTAK02 obtained from the Cambridge structural database (B).

1666 and 1699 cm^{-1} (Kazbanov et al., 2001; Ray et al., 2016). The peaks appeared at 521 and 618 cm^{-1} were associated with vibrations of Pt-N bond (Ray et al., 2016). The observed peaks at 1378 and 1318 cm^{-1} were ascribed to ν(C-O) and ν(C-C). The peaks at 811, 776 and 575 cm^{-} were ascribed to δ(COO) and Pt-O vibrations or their combination forms (Wysokiński et al., 2006). U(OX) and FU(OX), showed the typical vibrations of C-H that appeared between 2860 and 2990 cm^{-1} in the FTIR spectrum of OX (Wang et al., 2017; Cao et al., 2018b). U(OX) and FU (OX) showed the presence of a new vibration at 1693 and 1694 cm^{-1} respectively, which was attributed to $\nu(COO^{-})_{sym}$ of OX.

Powder X-ray diffraction (PXRD) patterns of the products were obtained and matched the simulated one (Reference code: RUBTAK02) as displayed in Fig. 2,**B** (Valenzano et al., 2011). The reflection planes including (111), (200), (222), (400), (331), (420), (333), (440), (600), (711), and (731) placed at 2θ of 7.3, 8.6, 14.8, 17.1, 18.6, 19.2, 22.3, 24.3, 25.8, 30.8 and 33.1° are associated with the simulated pattern obtained from crystal information file (CIF). The sharp intensities of peaks and the position of reflection planes showed the structural integrity after FA doping. PXRD patterns of U(OX) and FU(OX) proved that the loading does not influence the integrity of MOF. The FWHMs were used to obtain the changes in crystallite sizes after drug loading. The obtained crystallite sizes, which were calculated by the scherrer

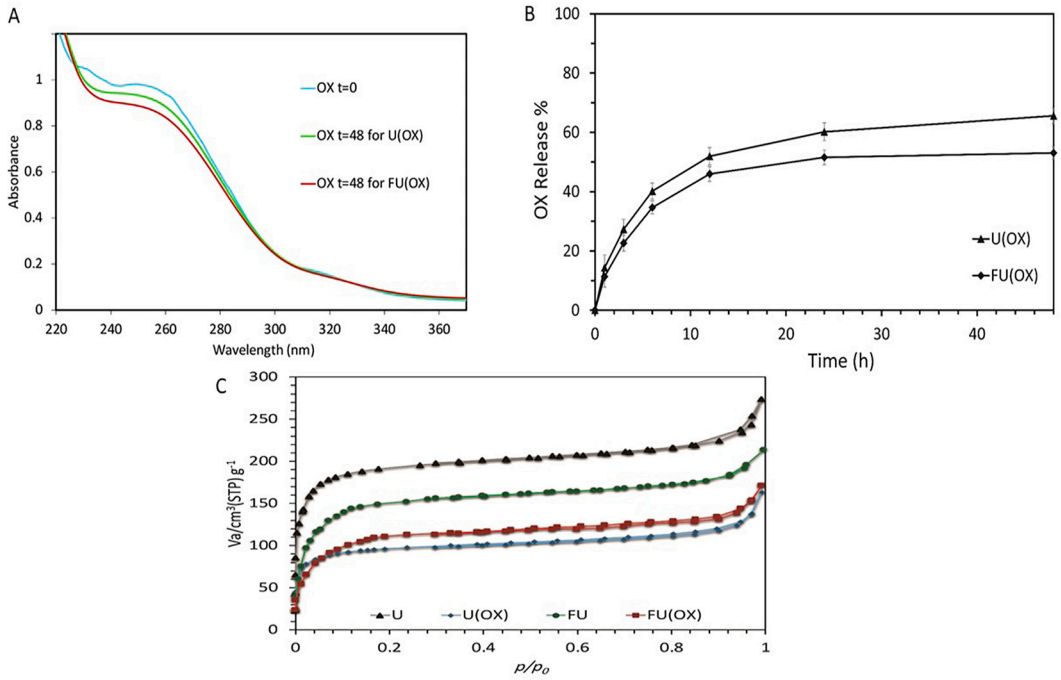

Fig. 3. Absorbance measurements of OX before and after loading in U and FU by UV–Vis spectrophotometry (A).The drug release measurements from U(OX) and FU (OX) against time (B).The BET analyses of U, U(OX), FU and FU(OX) (C).

equation, were 30.5, 34.6, 23.09 and 17.6 nm for U, U(OX), FU and FU (OX) respectively.

For drug encapsulation, the OX was impregnated using activated MOF in deionized water. After loading, the prepared nanodrugs were dispersed in a 5% dextrin solution. For drug loading, the maximum absorbance at $\lambda_{max} = 252$ nm was used to obtain the following equation: $A = 0.0015\ c + 0.0111$ (A: absorbance and c: concentration, Fig. 3**,A**). There is also potential absorbance from both the ligand and folic acid, hence unloaded MOFs were used and treated in similar conditions as the baseline to cancel the effect of possible detached molecules from the MOF under the loading conditions. Therefore, overlapping absorbance would be minimized in drug loading and preventing the overestimation of the clinical potential of the DDS. The evaluated amounts for U and FU were calculated 304.5 mg and 293.0 mg per 1 g respectively, which were equal to 30.4% and 29.3% of OX loading. ICP-OES of the supernatant after loading also confirms the above results (32.9% for U and 26.1% for FU.

The drug release profiles in 48 h for both U(OX) and FU(OX) were measured (shown in Fig. 3**,B**). PBS or culture medium was not used due to the instability of OX in chlorine-containing solutions (Mehta et al., 2015). It appears that the hydrophilic nature of both U and OX (Screnci et al., 2000) could influence the amount of drug loading and release mechanism (Zhang et al., 2017a). The initial burst releases of OX were 15.7% in U(OX) and 10.8% FU(OX) per hour. The releases have reached a plateau at 62.9% and 52.3% for U(OX) and FU(OX), respectively. The incomplete drug release might be due to drug entrapment into the pores, O…H-N hydrogen bond with O atom of OX and NH_2 group on U and FU or medium conditions.

Brunauer-Emmett-Teller (BET) analyses showed the changes in surface area, pore sizes and total pore volumes (Fig. 3**,C,** Table 3**)**. Analyses showed a type II isotherm for curves. After drug loading, surface area and pore sizes were decreased, indicating that OX could penetrate the pores.

FESEM images showed the morphological changes at different stages and were used to analyze the influence of drug loading on U and FU (Fig. 4**,A**). It appears that the semi-spherical morphology was maintained after loading. Furthermore, the size distribution appeared to be between ~50 to ~200 nm. According to FESEM images, the changes in diameter were not significant after loading. The sizes(±S.E.M.) were estimated as follows: U: 105.39 ± 1.35 nm, U(OX): 128.37 ± 1.89 nm, FU: 118.83 ± 1.67 nm and FU(OX): 115.15 ± 1.97 nm. FESEM images (Fig. 4**,A**) clearly showed that the doping of FA and drug loading did not change the morphologies significantly. The Full width at half-maximum (FWHM) displayed that the size distribution was increased for U(OX) (FWHM = 82.16) in comparison to U (FWHM = 59.93), but the change in FWHM of FU after loading was not significant. Because of the appearance of new interactions between oxaliplatin and U (or FU) and stiring, the transformation of grains to crytalites and the aggregation of particles may occur, which could cause the broadening of the FWHM and the increase in the range of the particles. The sizes in FESEM images showed agglomeration and were more than three times larger than the crystallite sizes. The boundary images of particles (grain sizes) from FESEM are usually less than the crystallite size obtained from the scherer equation using PXRD. The grain size indicated that each particle may contain at least 3 to 6 crystallites.

At the same time, energy-dispersive X-ray (EDX) analyzed and EDX mapping confirmed the elemental composition of U(OX) and FU(OX) without known peak related to any impurities. In the case of U(OX) and FU(OX), Pt transitions including PtMα, PtMβ, and PtLα displayed the presence of OX (Fig. 4**,B-a, c**). The spatial distribution of OX was analyzed by EDX mapping, which showed OX was well dispersed in both U and FU (Fig. 4B**- b, d**).

Dynamic light scattering (DLS) was used to analyze the changes in size after OX loading (Fig. 5**,** Table 4). 25 μg mL^{-1} of each sample was prepared for DLS analyses. The particles were completely dispersible in water and culture medium, which remain unchanged for at least a week. According to the results, sizes were increased comparatively in water and culture medium against dry sizes obtained from FESEM images. It was reported that hydrodynamic sizes were usually biased towards larger particles or indicating aggregates (Raj et al., 2016). Corona formation is another reason that led to an increase in size in the culture medium (Mahmoudi et al., 2011; Monopoli et al., 2011; Yu et al., 2013). Results showed that hydrodynamic sizes of FU and FU(OX) were changed dramatically. The size of FU in water was 2.4 times larger than its solid size, and subsequently 4.3 times in culture medium. A similar trend was observed for FU(OX) in water and culture medium. It is important to note that zeta potentials for U and FU were positive as expected, but they got negative after OX loading. Lower positivity in the zeta potential of FU (14.6 mV) than U (21.2) might be due to the surface functionalization of U with FA, which led to less available amino groups in contact with the solvent. The negativity observed in drug-loaded DDSs might be caused by the anchored OX on the external surface. In the growth medium, aggregation is a common phenomenon due to corona formation in the presence of proteins but it can increase the colloidal stability (Bellido et al., 2014). Corona formation or ionic strength could also balance the overall zeta potentials in the culture medium. The results showed that zeta potentials of the particles in growth media were slightly negative. This could not affect the functionality of the DDSs in vivo because of the acidic conditions of solid tumors. In acidic environments, amine groups usually get positive, leading to better interactions with the negatively charged cell membranes.

The MTT assay was used to predict the cytotoxicy of OX, U(OX), and FU(OX) on colorectal CT-26 cancer cells. During this process, the cells were exposed to the increasing concentrations of OX, U(OX)**,** and FU (OX) (0.001 to 1000 μg/mL) for 24 h (Fig. 6**,A**). The MTT test highlighted that nanoparticles, alone, had no significant cytotoxicity, but for FU(OX) cell death was significantly increased. To compare the cytotoxity of OX, U(OX)**,** and FU(OX), the half-maximal inhibitory concentrations (IC_{50}) were calculated at 24 h, which were 21.38, 95.50, and 18.20 μg/mL respectively. The IC50 of U(OX) and FU(OX) with the amount of oxaliplatin loading were 28.9 and 5.33 μg/mL accordingly. The IC50 of FU(OX) was one-quarter of OX, which shows its efficacy. The functionalization with FA enhanced the uptake of nanoparticles into CT-26 cells, hence the particles exhibited higher toxicity. The results were in line with our hypothesis of increased cytotoxicity by using FA as a targeting agent.

To investigate more, we used three other tests including migration assay, spheroid test and oxidative stress to confirm the MTT results. In the first attempt, a scratch assay was used to find the impression of U (OX) and FU(OX) on cell migration(Fig. 6**,A**). The scratched area was photographed every day, then the changes were calculated by the ImageJ software, and finally, the groups were compared. The results showed that the gap between the cells was filled by the migratory cells after 4 days in the control groups, while this process was not noticeable in treated groups. FU(OX) was shown to be more efficient in comparison with other groups (Fig. 6**,B**). Therefore, the data confirms that FU(OX), at 500 μg/mL, prevented migration better than U(OX).

Next, a spheroid assay was used to examine the anti-cancer capacity of U(OX) and FU(OX) in proportion with OX in a three dimensional (3-D) cellular structure. Although the spheroid size is not an appropriate measurement for cell proliferation, it was reported because it is

Table 3
Surface area, pore size, and total pore volume of U, U(OX), FU and FU (OX).

Sample	Surface area [m^2/g]	Pore size [Å]	Total pore volume [$p/p_0 = 0.990$]
U	714.93	12.2	0.4205
U(OX)	357.74	10.64	0.2501
FU	573.39	9.87	0.3381
FU(OX)	376.14	7.38	0.2167

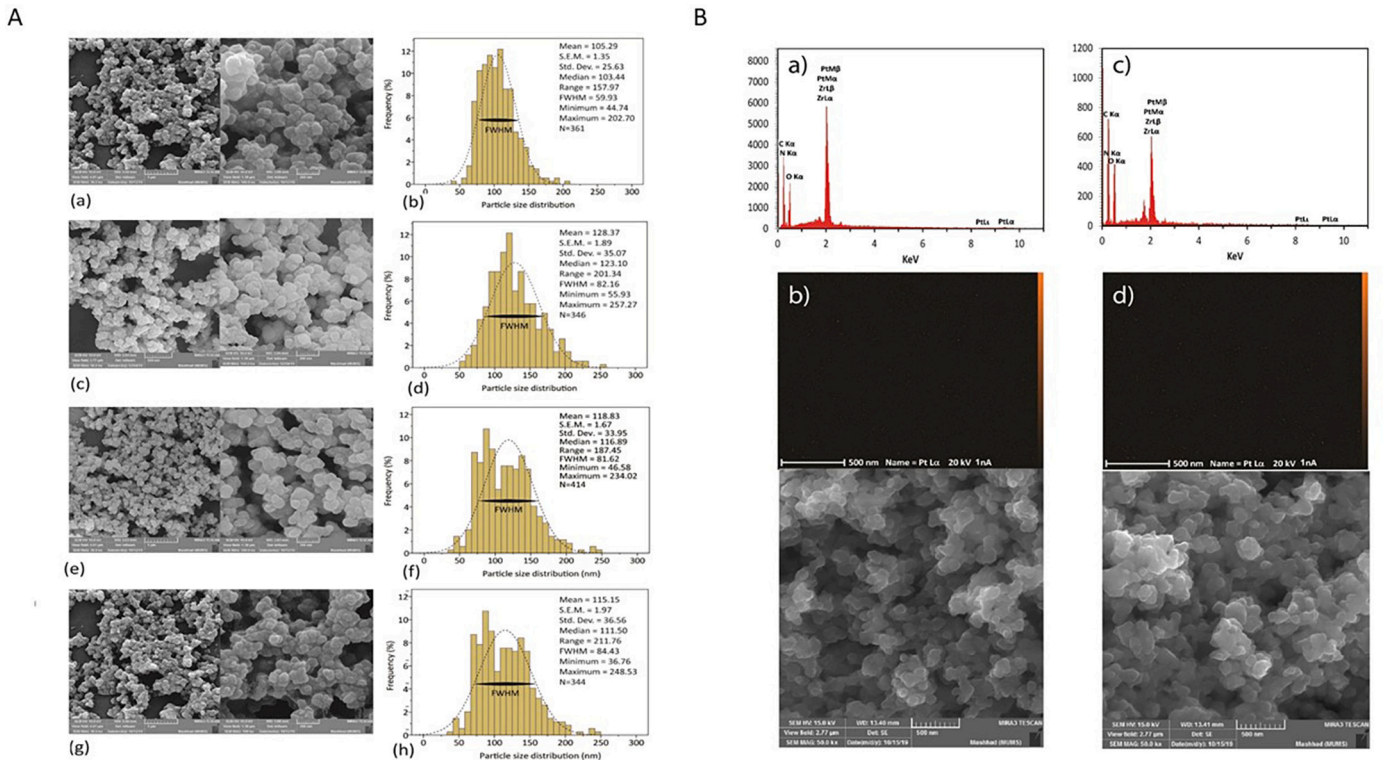

Fig. 4. FESEM images and size distribution of (a), (b) U with magnifications of 1 μm and 200 nm, (c), (d) U(OX) with magnifications of 500 nm and 200 nm, (e), (f) FU with magnifications of 1 μm and 200 nm, and (g), (h) FU(OX) with magnifications of 1 μm and 200 nm (A), the particle sizes were measured by ImageJ software and the frequencies (particle size distribution) were analyzed by SPSS software using descriptive statistics. The elemental composition of the nano drugs and platinum spatial distribution using EDX and EDX mapping of (a), (b) U(OX), and (c), (d) FU(OX) and their corresponding SE images (B) with a magnification of 500 nm by a TESCAN Mira 3 LMU device.

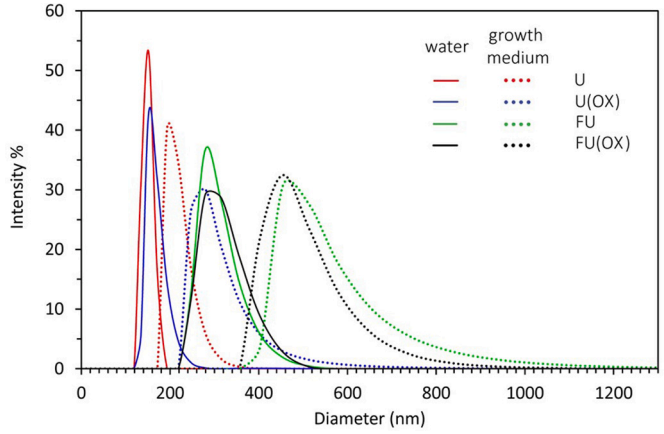

Fig. 5. DLS size analyses of U, U(OX), FU and FU(OX) in water and culture medium.

compatible with the previous results. After spheroid formation, they were treated with two doses of nanodrugs (500 and 50 μg/mL) and 20 μM of OX (Fig. 6,**C**). After three days, we observed noteworthy differences between the sizes of the spheroids in treated and control groups. The obtained results showed that treatments could diminish the proliferation and progression ability of CRC cells in three-dimensional models. It was also found that FU(OX) was more effective than OX and U(OX) in inhibiting cell proliferation in the 3D-model of cell culture (Fig. 6,**C**). In more detail, the sizes of the spheroids were decreased in the following manner: FU(OX) at 50 μg/mL < U(OX) at 50 μg/mL < U(OX) at 500 μg/mL ≅ FU(OX) at 500 μg/mL < OX 20 μM < control. It appears that FU(OX) can compete with OX and displays higher inhibition rates toward CT-26 cells in both cell migration and spheroid tests, which could confirm the applicability of the folate conjugated form. It is possible that FU(OX) would be superior in vivo. It should be noted that the size of spheroids can be generally reduced over time, but the size reduction showed the same phenomenon that was observed in the MTT assay.

Moreover, oxidative stress analyses were performed to investigate ROS production. The oxidative stress in the cancer cells is expressed by the imbalance in the systemic expression of ROS and the antioxidant

Table 4
Average particle size and zeta potential of U, U(OX), FU and FU(OX).

	Particle Size [nm]				Zeta Potential [mV]	
	PXRD	FESEM	DLS			
	Crystallite size	Solid	Water	Culture medium	Water	Culture medium
U	30.5	105.3 ± 25.6	157.5 ± 22.4	206.1 ± 27.4	21.2	−1.3
U(OX)	34.6	128.4 ± 35.1	160.3 ± 81.2	289.9 ± 68.1	−38	−2.2
FU	23.1	118.8 ± 33.9	289.5 ± 44.5	519.3 ± 118.0	14.6	−3.2
FU(OX)	17.6	115.1 ± 36.6	297.9 ± 47.6	468.1 ± 86.7	−22.8	−3.5

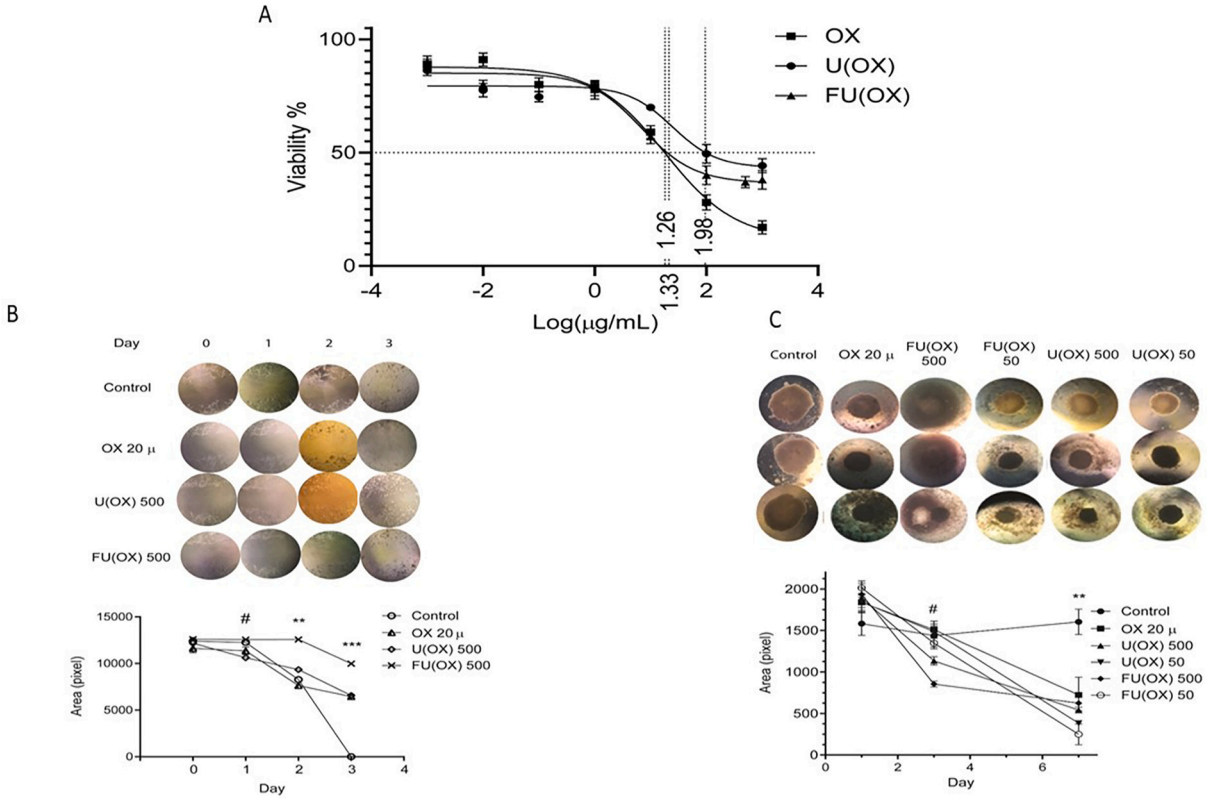

Fig. 6. FU(OX) and U(OX) reduce cell growth and proliferation in colorectal cancer cells.)Growing inhibitory properties of U(OX), FU(OX), and OX were studied after 24 h in CT26 cells. MTT tests were performed in triplicate ((A). Results of the scratch assay of FU(OX), U(OX), and OX in CT-26 cells. The scratch assay was performed in triplicate ($p < 0.01$). Inhibition of cancer cell migration increase statistically in FU(OX) treated cells in comparison to control after 3 days (B). After treatment of CT26 spheroids with OX, U(OX), and FU(OX) at 5xIC_{50} concentration. (b) a comparison of spheroid size was shown after 7 days. The growth of spheroids treated with OX, U(OX), and FU(OX) was decreased in comparison to the control group (C). Data are expressed as Mean ± SEM and differences are considered to be statistically significant at $P < 0.05$ using One-way analysis of variance (ANOVA), and LSD multiple comparisons test. All data was obtained from three independent experiments.

defense mechanisms (Soleimani et al., 2019). Oxidative stress and antioxidant metabolism have critical roles in the progression of CRC (Asadi-Samani et al., 2019). Most forms of chemotherapy rely on the generation of oxidative stress, a strategy that can cause cancer cell death. Several studies have argued that increased levels of ROS can cause cancer cell apoptosis,therefore can be led to the treatment of cancer (Asadi-Samani et al., 2019). In the present study, MDA as lipid peroxides in FU(OX), U(OX), and OX groups was increased compared to control. During chemotherapy, the key reason for elevated cellular ROS production is the inhibition of the antioxidant system such as SOD and SH-group (Afrin et al., 2019). Various studies have also shown that tumor cell growth is reduced by a decrease in the antioxidant defense system (Xu et al., 2017), our study also confirms this claim. Among OX and nanodrugs, the results showed FU(OX) could better induce ROS and disrupt the antioxidant system, which means, in theory, it should prevent cancer progression better than U(OX) or OX (Fig. 7**,A-C**).

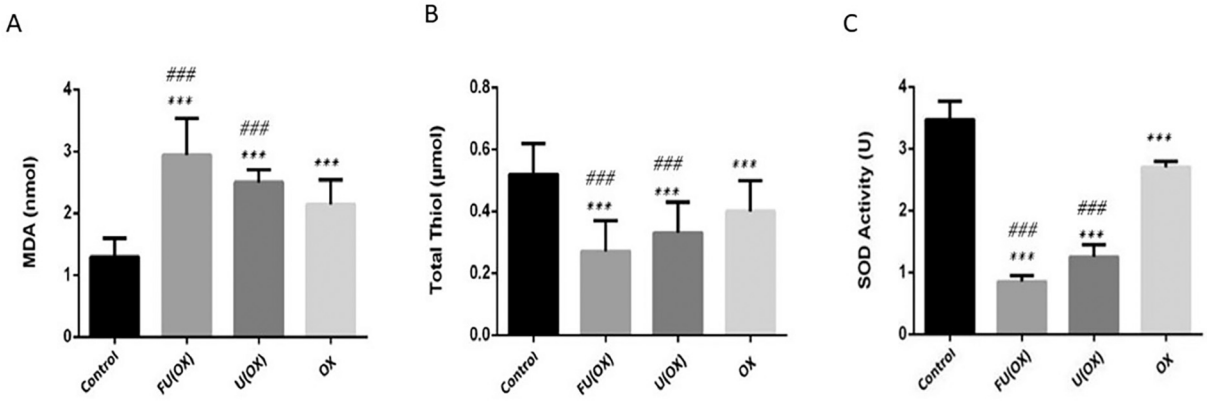

Fig. 7. Intracellular ROS production after treatment or no treatment with U(OX), FU(OX), and OX were explored by measurements of MDA activity, total thiol group, and SOD activity in colorectal cancer cells. Data are expressed as Mean ± SEM and differences are considered to be statistically significant at $P < 0.05$ using One-way analysis of variance (ANOVA), and LSD multiple comparisons test. All data was obtained from three independent experiments. ***$P < 0.001$ compared to control and and ###$P < 0.001$ compared to OX group.

4. Conclusion

In summary, UIO-66-NH_2 and FA functionalized UIO-66-NH_2 was realized as a new active drug transport system in oxaliplatin delivery against colorectal cancer cells. FU(OX) showed excellent receptor-specific targeting for folate receptor-positive colon cancer cells in MTT, spheroid model, cell migration and oxidative features. FU(OX) had a higher inhibitory effect on proliferation compared to OX and U(OX), which could confirm the applicability of the folate conjugated form. FU (OX) could induce higher levels of ROS in comparison with oxaliplatin and U(OX). The results obtained from the spheroid model and the cell migration have also confirmed the superiority of FU(OX) compared to oxaliplatin. Such drug delivery systems could be used and verified in biomedical applications in colorectal cancer animal models, which will be done in future studies. Moreover, this research could be an initiative to treat CRC patients using non-toxic and biocompatible MOFs.

Data availability

The authors declare that all data supporting the findings of this study are available within the paper.

Author contributions

Dr. Alireza Hashemzadeh was initiated, designed and executed the project and finally drafted the manuscript. The cellular experiments were performed and written by Frouzan Amerizadeh. The Oxidation stress tests were done and written by Fereshteh Asgharzadeh. Mohammad Landarani was partially contributed in data analyses. The whole project including the study and performed experiments was supervised by Prof. Majid Khazaei. He also provided all the chemicals, equipment and funds. Dr. Amir Avan, Dr. Seyed Mahdi Hassanian and Dr. Majid Daroudi were both consultants of this project. Dr. Amir Avan also supervised cellular experiments.

Funding sources

This work financially supported by National Institute for Medical Research Development (*NIMAD*) through grant # 982641, Iran National Science Foundation (*INSF*) through grant # 97017412 and Mashhad University of Medical Sciences (MUMS) through grant # 971010 as a research project.

Author statement

All authors are aware of and agree to the content of the manuscript. Neither the submitted paper, nor any similar article, either in whole or in part, have been or will be submitted or published in any other scientific journal. The authors have indicated no potential conflicts of interest in this study.

Declaration of Competing Interest

The authors have no conflicts of interest to declare.

Acknowledgments

This study was supported by Elite Researcher Grant Committee under award number #982641 from the National Institute for Medical Research Development (NIMAD) and grant number # 97017412 from Iran National Science Foundation (INSF).

References

Abánades Lázaro, I., Haddad, S., Rodrigo-Muñoz, J.M., Marshall, R.J., Sastre, B., del Pozo, V., Fairen-Jimenez, D., Forgan, R.S., 2018a. Surface-functionalization of Zr-fumarate MOF for selective cytotoxicity and immune system compatibility in nanoscale drug delivery. ACS Appl. Mater. Interfaces 10, 31146–31157.

Abánades Lázaro, I., Haddad, S., Rodrigo-Muñoz, J.M., Orellana-Tavra, C., del Pozo, V., Fairen-Jimenez, D., Forgan, R.S., 2018b. Mechanistic investigation into the selective anticancer cytotoxicity and immune system response of surface-functionalized, dichloroacetate-loaded, UiO-66 nanoparticles. ACS Appl. Mater. Interfaces 10, 5255–5268.

Abánades, L.I., Haddad, S., Rodrigo-Muñoz, J., Marshall, R., Sastre, B., Del Pozo, V., Fairen-Jimenez, D., Forgan, R., 2018. Surface-functionalization of Zr-fumarate MOF for selective cytotoxicity and immune system compatibility in nanoscale drug delivery. ACS Appl. Mater. Interfaces 10, 31146.

Afrin, S., Forbes-Hernández, T.Y., Cianciosi, D., Pistollato, F., Zhang, J., Pacetti, M., Amici, A., Reboredo-Rodríguez, P., Simal-Gandara, J., Bompadre, S., 2019. Strawberry tree honey as a new potential functional food. Part 2: Strawberry tree honey increases ROS generation by suppressing Nrf2-ARE and NF-κB signaling pathways and decreases metabolic phenotypes and metastatic activity in colon cancer cells. J. Funct. Foods 57, 477–487.

Agrahari, B., Layek, S., Kumari, S., Ganguly, R., Pathak, D.D., 2017. Synthesis, characterization and crystal structure of Cu (II) complex of trans-cyclohexane-1, 2-diamine: Application in synthesis of symmetrical biaryls. J. Mol. Struct. 1134, 85–90.

Asadi-Samani, M., Farkhad, N.K., Mahmoudian-Sani, M.R., Shirzad, H., 2019. Antioxidants as a Double-Edged Sword in the Treatment of Cancer, Antioxidants. IntechOpen.

Asgharzadeh, F., Bargi, R., Beheshti, F., Hosseini, M., Farzadnia, M., Khazaei, M., 2017. Thymoquinone restores liver fibrosis and improves oxidative stress status in a lipopolysaccharide-induced inflammation model in rats. Avicenna J. Phytomed. 7, 502.

Au, K.M., Satterlee, A., Min, Y., Tian, X., Kim, Y.S., Caster, J.M., Zhang, L., Zhang, T., Huang, L., Wang, A.Z., 2016. Folate-targeted pH-responsive calcium zoledronate nanoscale metal-organic frameworks: Turning a bone antiresorptive agent into an anticancer therapeutic. Biomaterials 82, 178–193.

Bahrami, J., Khazaei, M., Hassanian, S.M., Shahidsales, S., Joudi-Mashhad, Mona, Maftouh, M., Jazayeri, M., Parizade, Mohammad reza, Ferns, G., Avan, A., 2018. Targeting the tumor microenvironment as a potential therapeutic approach in colorectal cancer: Rational and progress. Journal of Cellular Physiology 233 (4), 2928–2936.

Bai, Y., Dou, Y., Xie, L.-H., Rutledge, W., Li, J.-R., Zhou, H.-C., 2016. Zr-based metal–organic frameworks: design, synthesis, structure, and applications. Chem. Soc. Rev. 45, 2327–2367.

Bansal, D., Gulbake, A., Tiwari, J., Jain, S.K., 2016. Development of liposomes entrapped in alginate beads for the treatment of colorectal cancer. Int. J. Biol. Macromol. 82, 687–695.

Bargi, R., Asgharzadeh, F., Beheshti, F., Hosseini, M., Sadeghnia, H.R., Khazaei, M., 2017. The effects of thymoquinone on hippocampal cytokine level, brain oxidative stress status and memory deficits induced by lipopolysaccharide in rats. Cytokine 96, 173–184.

Bellido, E., Guillevic, M., Hidalgo, T., Santander-Ortega, M.J., Serre, C., Horcajada, P., 2014. Understanding the colloidal stability of the mesoporous MIL-100 (Fe) nanoparticles in physiological media. Langmuir 30, 5911–5920.

Boddu, S.H., Vaishya, R., Jwala, J., Vadlapudi, A., Pal, D., Mitra, A., 2012. Preparation and characterization of folate conjugated nanoparticles of doxorubicin using PLGA-PEG-FOL polymer. Med. Chem. 2, 68–75.

Brown, S.D., Nativo, P., Smith, J.-A., Stirling, D., Edwards, P.R., Venugopal, B., Flint, D. J., Plumb, J.A., Graham, D., Wheate, N.J., 2010. Gold nanoparticles for the improved anticancer drug delivery of the active component of oxaliplatin. J. Am. Chem. Soc. 132, 4678–4684.

Cai, W., Wang, J., Chu, C., Chen, W., Wu, C., Liu, G., 2019. Metal–Organic Framework-Based Stimuli-Responsive Systems for Drug Delivery. Adv. Sci. 6, 1801526.

Cao, J., Chen, Z., Chi, J., Sun, Y., Sun, Y., 2018a. Recent progress in synergistic chemotherapy and phototherapy by targeted drug delivery systems for cancer treatment. Artif. Cells Nanomed. Biotechnol. 46, 817–830.

Cao, Y., Zhang, H., Song, F., Huang, T., Ji, J., Zhong, Q., Chu, W., Xu, Q., 2018b. UiO-66-NH2/GO Composite: Synthesis, Characterization and CO2 Adsorption Performance.

Chen, F., Ehlerding, E.B., Cai, W., 2014. Theranostic nanoparticles. J. Nucl. Med. 55, 1919–1922.

Chowdhuri, A.R., Bhattacharya, D., Sahu, S.K., 2016a. Magnetic nanoscale metal organic frameworks for potential targeted anticancer drug delivery, imaging and as an MRI contrast agent. Dalton Trans. 45, 2963–2973.

Chowdhuri, A.R., Laha, D., Pal, S., Karmakar, P., Sahu, S.K., 2016b. One-pot synthesis of folic acid encapsulated upconversion nanoscale metal organic frameworks for targeting, imaging and pH responsive drug release. Dalton Trans. 45, 18120–18132.

Chowdhuri, A.R., Singh, T., Ghosh, S.K., Sahu, S.K., 2016c. Carbon dots embedded magnetic nanoparticles@ chitosan@ metal organic framework as a nanoprobe for pH sensitive targeted anticancer drug delivery. ACS Appl. Mater. Interfaces 8, 16573–16583.

Chowdhuri, A.R., Das, B., Kumar, A., Tripathy, S., Roy, S., Sahu, S.K., 2017a. One-pot synthesis of multifunctional nanoscale metal-organic frameworks as an effective antibacterial agent against multidrug-resistant Staphylococcus aureus. Nanotechnology 28, 095102.

Chowdhuri, A.R., Laha, D., Chandra, S., Karmakar, P., Sahu, S.K., 2017b. Synthesis of multifunctional upconversion NMOFs for targeted antitumor drug delivery and imaging in triple negative breast cancer cells. Chem. Eng. J. 319, 200–211.

Clemons, T.D., Singh, R., Sorolla, A., Chaudhari, N., Hubbard, A., Iyer, K.S., 2018. Distinction between active and passive targeting of nanoparticles dictate their overall therapeutic efficacy. Langmuir 34, 15343–15349.

Coppede, F., 2014. Epigenetic biomarkers of colorectal cancer: focus on DNA methylation. Cancer Lett. 342, 238–247.
Dai, L., Liu, J., Luo, Z., Li, M., Cai, K., 2016. Tumor therapy: targeted drug delivery systems. J. Mater. Chem. B 4, 6758–6772.
D'angelica, M., Ammori, J., Gonen, M., Klimstra, D.S., Low, P.S., Murphy, L., Weiser, M. R., Paty, P.B., Fong, Y., DeMatteo, R.P., 2011. Folate receptor-α expression in resectable hepatic colorectal cancer metastases: patterns and significance. Mod. Pathol. 24, 1221–1228.
Dong, H., Yang, G.X., Zhang, X., Meng, X.B., Sheng, J.L., Sun, X.J., Feng, Y.J., Zhang, F. M., 2018. Folic Acid Functionalized Zirconium-Based Metal–Organic Frameworks as Drug Carriers for Active Tumor-Targeted Drug Delivery. Chem. Eur. J. 24, 17148–17154.
Fan, N.C., Cheng, F.Y., Ho, J.A.A., Yeh, C.S., 2012. Photocontrolled targeted drug delivery: photocaged biologically active folic acid as a light-responsive tumor-targeting molecule. Angew. Chem. Int. Ed. 51, 8806–8810.
Faust, T., 2015. Nanomedicine: MOFs deliver. Nat. Chem. 7, 270.
Gao, X., Hai, X., Baigude, H., Guan, W., Liu, Z., 2016. Fabrication of functional hollow microspheres constructed from MOF shells: Promising drug delivery systems with high loading capacity and targeted transport. Sci. Rep. 6, 37705.
Gao, X., Zhai, M., Guan, W., Liu, J., Liu, Z., Damirin, A., 2017. Controllable synthesis of a smart multifunctional nanoscale metal–organic framework for magnetic resonance/optical imaging and targeted drug delivery. ACS Appl. Mater. Interfaces 9, 3455–3462.
Gao, X., Cui, R., Ji, G., Liu, Z., 2018. Size and surface controllable metal–organic frameworks (MOFs) for fluorescence imaging and cancer therapy. Nanoscale 10, 6205–6211.
Handali, S., Moghimipour, E., Rezaei, M., Saremy, S., Dorkoosh, F.A., 2019. Co-delivery of 5-fluorouracil and oxaliplatin in novel poly (3-hydroxybutyrate-co-3-hydroxyvalerate acid)/poly (lactic-co-glycolic acid) nanoparticles for colon cancer therapy. Int. J. Biol. Macromol. 124, 1299–1311.
Hartmann, L.C., Keeney, G.L., Lingle, W.L., Christianson, T.J., Varghese, B., Hillman, D., Oberg, A.L., Low, P.S., 2007. Folate receptor overexpression is associated with poor outcome in breast cancer. Int. J. Cancer 121, 938–942.
Hashemzehi, M., Rahmani, F., Khoshakhlagh, M., Avan, A., Asgharzadeh, F., Barneh, F., Moradi-Marjaneh, R., Soleimani, A., Fiuji, H., Ferns, G.A., 2021. Angiotensin receptor blocker Losartan inhibits tumor growth of colorectal cancer. EXCLI J. 20, 506–521.
Horcajada, P., Chalati, T., Serre, C., Gillet, B., Sebrie, C., Baati, T., Eubank, J.F., Heurtaux, D., Clayette, P., Kreuz, C., 2010. Porous metal–organic-framework nanoscale carriers as a potential platform for drug delivery and imaging. Nat. Mater. 9, 172.
Ibrahim, M., Sabouni, R., Husseini, A., 2017. Anti-cancer drug delivery using metal organic frameworks (MOFs). Curr. Med. Chem. 24, 193–214.
Jiang, W., Zhang, H., Wu, J., Zhai, G., Li, Z., Luan, Y., Garg, S., 2018. CuS@ MOF-based well-designed quercetin delivery system for chemo–photothermal therapy. ACS Appl. Mater. Interfaces 10, 34513–34523.
Kalli, K.R., Oberg, A.L., Keeney, G.L., Christianson, T.J., Low, P.S., Knutson, K.L., Hartmann, L.C., 2008. Folate receptor alpha as a tumor target in epithelial ovarian cancer. Gynecol. Oncol. 108, 619–626.
Katz, M.J., Brown, Z.J., Colón, Y.J., Siu, P.W., Scheidt, K.A., Snurr, R.Q., Hupp, J.T., Farha, O.K., 2013. A facile synthesis of UiO-66, UiO-67 and their derivatives. Chem. Commun. 49, 9449–9451.
Kazbanov, V., Starkov, A., Kozhukhovskaya, G., Kazbanova, T., Trofimov, V., Pavlenko, N., 2001. Study of the structure and reactions of bis (μ-Oxalato) tetramminediplatinum (II) in aqueous chloride solutions. Russ. J. Coord. Chem. 27, 65–69.
Khoshgard, K., Hashemi, B., Arbabi, A., Rasaee, M.J., Soleimani, M., 2014. Radiosensitization effect of folate-conjugated gold nanoparticles on HeLa cancer cells under orthovoltage superficial radiotherapy techniques. Phys. Med. Biol. 59, 2249.
Kue, C.S., Kamkaew, A., Burgess, K., Kiew, L.V., Chung, L.Y., Lee, H.B., 2016. Small molecules for active targeting in cancer. Med. Res. Rev. 36, 494–575.
Laha, D., Pal, K., Chowdhuri, A.R., Parida, P.K., Sahu, S.K., Jana, K., Karmakar, P., 2019. Fabrication of curcumin-loaded folic acid-tagged metal organic framework for triple negative breast cancer therapy in in vitro and in vivo systems. New J. Chem. 43, 217–229.
Lai, C., Yu, X., Zhuo, H., Zhou, N., Xie, Y., He, J., Peng, Y., Xie, X., Luo, G., Zhou, S., 2014. Anti-tumor immune response of folate-conjugated chitosan nanoparticles containing the IP-10 gene in mice with hepatocellular carcinoma. J. Biomed. Nanotechnol. 10, 3576–3589.
Lazaro, I.A., Forgan, R.S., 2019. Application of zirconium MOFs in drug delivery and biomedicine. Coord. Chem. Rev. 380, 230–259.
Li, M., Huang, Y., Yu, T., Chen, S., Ju, A., Ge, M., 2014. Chemical recycling of waste poly (ethylene terephthalate) fibers into azo disperse dyestuffs. RSC Adv. 4, 46476–46480.
Li, H., Cheng, Y., Liu, Y., Chen, B., 2016a. Fabrication of folic acid-sensitive gold nanoclusters for turn-on fluorescent imaging of overexpression of folate receptor in tumor cells. Talanta 158, 118–124.
Li, Y.-A., Zhao, X.-D., Yin, H.-P., Chen, G.-J., Yang, S., Dong, Y.-B., 2016b. A drug-loaded nanoscale metal–organic framework with a tumor targeting agent for highly effective hepatoma therapy. Chem. Commun. 52, 14113–14116.
Liu, J., Zhang, L., Lei, J., Shen, H., Ju, H., 2017. Multifunctional Metal–Organic Framework Nanoprobe for Cathepsin B-Activated Cancer Cell Imaging and Chemo-Photodynamic Therapy. ACS Appl. Mater. Interfaces 9, 2150–2158.
Madesh, M., Balasubramanian, K., 1998. Microtiter plate assay for superoxide dismutase using MTT reduction by superoxide. Indian J. Biochem. Biophys. 35, 184–188.
Mahmoudi, M., Lynch, I., Ejtehadi, M.R., Monopoli, M.P., Bombelli, F.B., Laurent, S., 2011. Protein– nanoparticle interactions: opportunities and challenges. Chem. Rev. 111, 5610–5637.
Marcato, P.D., 2014. Pharmacokinetics and pharmacodynamics of nanomaterials. Nanotoxicology 97–110. Springer.
Markert, S., Lassmann, S., Gabriel, B., Klar, M., Werner, M., Gitsch, G., Kratz, F., Hasenburg, A., 2008. Alpha-folate receptor expression in epithelial ovarian carcinoma and non-neoplastic ovarian tissue. Anticancer Res. 28, 3567–3572.
Mehta, A., Van den Hoven, J., Rosing, H., Hillebrand, M., Nuijen, B., Huitema, A., Beijnen, J., Verwaal, V., 2015. Stability of oxaliplatin in chloride-containing carrier solutions used in hyperthermic intraperitoneal chemotherapy. Int. J. Pharm. 479, 23–27.
Miller, S.R., Heurtaux, D., Baati, T., Horcajada, P., Grenèche, J.-M., Serre, C., 2010. Biodegradable therapeutic MOFs for the delivery of bioactive molecules. Chem. Commun. 46, 4526–4528.
Monopoli, M.P., Bombelli, F.B., Dawson, K.A., 2011. Nanobiotechnology: nanoparticle coronas take shape. Nat. Nanotechnol. 6, 11.
Moore, K.N., Martin, L.P., O'Malley, D.M., Matulonis, U.A., Konner, J.A., Perez, R.P., Bauer, T.M., Ruiz-Soto, R., Birrer, M.J., 2017. Safety and activity of mirvetuximab soravtansine (IMGN853), a folate receptor alpha–targeting antibody–drug conjugate, in platinum-resistant ovarian, fallopian tube, or primary peritoneal cancer: a phase i expansion study. J. Clin. Oncol. 35, 1112.
Moore, K.N., O'Malley, D.M., Vergote, I., Martin, L.P., Gonzalez-Martin, A., Malek, K., Birrer, M.J., 2018. Safety and activity findings from a phase 1b escalation study of mirvetuximab soravtansine, a folate receptor alpha (FRα)-targeting antibody-drug conjugate (ADC), in combination with carboplatin in patients with platinum-sensitive ovarian cancer. Gynecol. Oncol. 151, 46–52.
Nam, N.H., Doan, D.H., Nhung, H.T.M., Quang, B.T., Nam, P.H., Thong, P.Q., Phuc, N.X., Thu, H.P., 2016. Folate attached, curcumin loaded Fe3O4 nanoparticles: A novel multifunctional drug delivery system for cancer treatment. Mater. Chem. Phys. 172, 98–104.
Nejadshafiee, V., Naeimi, H., Goliaei, B., Bigdeli, B., Sadighi, A., Dehghani, S., Lotfabadi, A., Hosseini, M., Nezamtaheri, M.S., Amanlou, M., 2019. Magnetic bio-metal–organic framework nanocomposites decorated with folic acid conjugated chitosan as a promising biocompatible targeted theranostic system for cancer treatment. Mater. Sci. Eng. C 99, 805–815.
Nguyen, D.T.D., Bach, L.G., Nguyen, T.H., Ho, M.H., Ho, M.N., Nguyen, D.H., Nguyen, C. K., Thi, T.T.H., 2019. Preparation and characterization of oxaliplatin drug delivery vehicle based on PEGylated half-generation PAMAM dendrimer. J. Polym. Res. 26, 116.
Onoue, S., Yamada, S., Chan, H.-K., 2014. Nanodrugs: pharmacokinetics and safety. Int. J. Nanomedicine 9, 1025.
Orellana-Tavra, C., Baxter, E.F., Tian, T., Bennett, T.D., Slater, N.K., Cheetham, A.K., Fairen-Jimenez, D., 2015. Amorphous metal–organic frameworks for drug delivery. Chem. Commun. 51, 13878–13881.
Orellana-Tavra, C., Marshall, R.J., Baxter, E.F., Lázaro, I.A., Tao, A., Cheetham, A.K., Forgan, R.S., Fairen-Jimenez, D., 2016a. Drug delivery and controlled release from biocompatible metal–organic frameworks using mechanical amorphization. J. Mater. Chem. B 4, 7697–7707.
Orellana-Tavra, C., Mercado, S.A., Fairen-Jimenez, D., 2016b. Endocytosis mechanism of nano metal-organic frameworks for drug delivery. Adv. Healthcare Mater. 5, 2261–2270.
Petrak, K., 2005. Essential properties of drug-targeting delivery systems. Drug Discov. Today 10, 1667–1673.
Raj, J.G.J., Quintanilla, M., Vetrone, F., 2016. Near-infrared triggered generation of reactive oxygen species from upconverting nanoparticles decorated with an organoiridium complex. J. Mater. Chem. B 4, 3113–3120.
Ray, S., Karmakar, P., Chattopadhyay, A., Nandi, D., Sarkar, R., Ghosh, A.K., 2016. Kinetic and mechanistic investigations on some N, N-Chelated Pt (II) oxalate complexes with some "S" containing biorelevant ligands at physiological condition. Int. J. Chem. Kinet. 48, 347–357.
Rosenholm, J.M., Sahlgren, C., Lindén, M., 2010. Towards multifunctional, targeted drug delivery systems using mesoporous silica nanoparticles–opportunities & challenges. Nanoscale 2, 1870–1883.
Samadian, H., Hosseini-Nami, S., Kamrava, S.K., Ghaznavi, H., Shakeri-Zadeh, A., 2016. Folate-conjugated gold nanoparticle as a new nanoplatform for targeted cancer therapy. J. Cancer Res. Clin. Oncol. 142, 2217–2229.
Screnci, D., McKeage, M.J., Galettis, P., Hambley, T.W., Palmer, B.D., Baguley, B.C., 2000. Relationships between hydrophobicity, reactivity, accumulation and peripheral nerve toxicity of a series of platinum drugs. Br. J. Cancer 82, 966–972.
Shia, J., Klimstra, D.S., Nitzkorski, J.R., Low, P.S., Gonen, M., Landmann, R., Weiser, M. R., Franklin, W.A., Prendergast, F.G., Murphy, L., 2008. Immunohistochemical expression of folate receptor α in colorectal carcinoma: patterns and biological significance. Hum. Pathol. 39, 498–505.
Simagina, A.A., Polynski, M.V., Vinogradov, A.V., Pidko, E.A., 2018. Towards rational design of metal-organic framework-based drug delivery systems. Russ. Chem. Rev. 87, 831.
Singh, R., Norret, M., House, M.J., Galabura, Y., Bradshaw, M., Ho, D., Woodward, R.C., Pierre, T.G.S., Luzinov, I., Smith, N.M., 2016. Dose-dependent therapeutic distinction between active and passive targeting revealed using transferrin-coated PGMA nanoparticles. Small 12, 351–359.
Soleimani, A., Asgharzadeh, F., Rahmani, F., Avan, A., Mehraban, S., Fakhraei, M., Arjmand, M.H., Binabaj, M.M., Parizadeh, M.R., Ferns, G.A., 2020 Feb. Novel oral transforming growth factor-β signaling inhibitor potently inhibits postsurgical adhesion band formation. J. Cell. Physiol. 235 (2), 1349–1357.

Steichen, S.D., Caldorera-Moore, M., Peppas, N.A., 2013. A review of current nanoparticle and targeting moieties for the delivery of cancer therapeutics. Eur. J. Pharm. Sci. 48, 416–427.
Sudimack, J., Lee, R.J., 2000. Targeted drug delivery via the folate receptor. Adv. Drug Deliv. Rev. 41, 147–162.
Thu, H.P., Nam, N.H., Quang, B.T., Son, H.A., Toan, N.L., Quang, D.T., 2015. In vitro and in vivo targeting effect of folate decorated paclitaxel loaded PLA–TPGS nanoparticles. Saudi Pharmaceut. J. 23, 683–688.
Toporkiewicz, M., Meissner, J., Matusewicz, L., Czogalla, A., Sikorski, A.F., 2015. Toward a magic or imaginary bullet? Ligands for drug targeting to cancer cells: principles, hopes, and challenges. Int. J. Nanomedicine 10, 1399.
Valenzano, L., Civalleri, B., Chavan, S., Bordiga, S., Nilsen, M.H., Jakobsen, S., Lillerud, K.P., Lamberti, C., 2011. Disclosing the complex structure of UiO-66 metal organic framework: a synergic combination of experiment and theory. Chem. Mater. 23, 1700–1718.
Varshosaz, J., Hassanzadeh, F., Sadeghi-Aliabadi, H., Firozian, F., 2014. Uptake of etoposide in CT-26 cells of colorectal cancer using folate targeted dextran stearate polymeric micelles. Biomed. Res. Int. **2014**.
Wang, Y., Wang, L., Huang, W., Zhang, T., Hu, X., Perman, J.A., Ma, S., 2017. A metal–organic framework and conducting polymer based electrochemical sensor for high performance cadmium ion detection. J. Mater. Chem. A 5, 8385–8393.
Weitman, S.D., Frazier, K.M., Kamen, B.A., 1994. The folate receptor in central nervous system malignancies of childhood. J. Neuro-Oncol. 21, 107–112.
Wu, M.X., Yang, Y.W., 2017. Metal–organic framework (MOF)-based drug/cargo delivery and cancer therapy. Adv. Mater. 29, 1606134.
Wu, X., Chen, J., Wu, M., Zhao, J.X., 2015. Aptamers: active targeting ligands for cancer diagnosis and therapy. Theranostics 5, 322.
Wu, M.-X., Yan, H.-J., Gao, J., Cheng, Y., Yang, J., Wu, J.-R., Gong, B.-J., Zhang, H.-Y., Yang, Y.-W., 2018. Multifunctional supramolecular materials constructed from polypyrrole@ UiO-66 nanohybrids and pillararene nanovalves for targeted chemophotothermal therapy. ACS Appl. Mater. Interfaces 10, 34655–34663.
Wysokiński, R., Kuduk-Jaworska, J., Michalska, D., 2006. Electronic structure, Raman and infrared spectra, and vibrational assignment of carboplatin, Density functional theory studies. J. Mol. Struct. THEOCHEM 758, 169–179.
Xu, J., Wise, J.T., Wang, L., Schumann, K., Zhang, Z., Shi, X., 2017. Dual roles of oxidative stress in metal carcinogenesis. J. Environ. Pathol. Toxicol. Oncol. 36.
Yang, B., Shen, M., Liu, J., Ren, F., 2017. Post-synthetic modification nanoscale metal-organic frameworks for targeted drug delivery in cancer cells. Pharm. Res. 34, 2440–2450.
Yu, Z., Reid, J.C., Yang, Y.-P., 2013. Utilizing dynamic light scattering as a process analytical technology for protein folding and aggregation monitoring in vaccine manufacturing. J. Pharm. Sci. 102, 4284–4290.
Yu, X., Trase, I., Ren, M., Duval, K., Guo, X., Chen, Z., 2016. Design of nanoparticle-based carriers for targeted drug delivery. J. Nanomater. 2016.
Zangabad, P.S., Karimi, M., Mehdizadeh, F., Malekzad, H., Ghasemi, A., Bahrami, S., Zare, H., Moghoofei, M., Hekmatmanesh, A., Hamblin, M.R., 2017. Nanocaged platforms: modification, drug delivery and nanotoxicity, Opening synthetic cages to release the tiger. Nanoscale 9, 1356–1392.
Zhang, L., Zhu, W., Yang, C., Guo, H., Yu, A., Ji, J., Gao, Y., Sun, M., Zhai, G., 2012. A novel folate-modified self-microemulsifying drug delivery system of curcumin for colon targeting. Int. J. Nanomedicine 7, 151.
Zhang, F., Sang, X., Tan, X., Liu, C., Zhang, J., Luo, T., Liu, L., Han, B., Yang, G., Binks, B. P., 2017a. Converting metal–organic framework particles from hydrophilic to hydrophobic by an interfacial assembling route. Langmuir 33, 12427–12433.
Zhang, H., Jiang, W., Liu, R., Zhang, J., Zhang, D., Li, Z., Luan, Y., 2017b. Rational design of metal organic framework nanocarrier-based codelivery system of doxorubicin hydrochloride/verapamil hydrochloride for overcoming multidrug resistance with efficient targeted cancer therapy. ACS Appl. Mater. Interfaces 9, 19687–19697.
Zhou, J., Yu, G., Huang, F., 2017. Supramolecular chemotherapy based on host–guest molecular recognition: a novel strategy in the battle against cancer with a bright future. Chem. Soc. Rev. 46, 7021–7053.
Zucolotto, V., 2013. Nanotoxicology: materials, methodologies, and assessments. Springer Science & Business Media.